Targeting Apollo-NADP$^+$ to image NADPH generation in pancreatic beta-cell organelles

Huntley H. Chang[a,b,1], Alexander M. Bennett[a,b,1], William D. Cameron[a,b], Eric Floro[a,b], Aaron Au[a], Christopher M. McFaul[a], Christopher M. Yip[a], Jonathan V. Rocheleau[a,b,c,d,2]

[a]Institute of Biomedical Engineering, University of Toronto, Toronto, ON M5S 3G9, Canada
[b]Toronto General Hospital Research Institute, University Health Network, Toronto, ON M5G 2C4, Canada
[c]Department of Physiology, University of Toronto, Toronto, ON M5S 1A8, Canada
[d]Banting and Best Diabetes Centre, University of Toronto, Toronto, ON M5G 2C4, Canada

[1]H.H.C and A.M.B. contributed equally to this work
[2]To whom correspondence may be addressed.

Corresponding Author: Jonathan V. Rocheleau
Rosebrugh Building, RM 407
164 College Street
Toronto, ON M5S 3G9
Phone: 416-581-7839
Email: jon.rocheleau@utoronto.ca

Author Contributions: H.H.C., A.M.B., W.D.C., and J.V.R. designed research; H.H.C., A.M.B., W.D.C., and E.F. performed research; H.H.C., A.M.B., W.D.C., and E.F. analyzed data; A.A., C.M.M., and C.M.Y provided technical expertise, and H.H.C. and J.V.R. wrote the paper.

Abstract:

NADPH/NADP$^+$ redox state supports numerous reactions related to cell growth and survival; yet the full impact is difficult to appreciate due to organelle compartmentalization of NADPH and NADP$^+$. Our goal here was to target the Apollo-NADP$^+$ sensor to measure glucose-stimulated NADPH production in pancreatic beta-cell organelles. To select the most pH stable version, we swapped various fluorescent proteins into the single colour sensor. We subsequently targeted the mTurquoise2 version of Apollo-NADP$^+$ and confirmed activity in the cytoplasm, mitochondrial matrix, nucleus, and peroxisome. We subsequently measured the glucose- and glutamine-stimulated NADPH responses by single and dual colour imaging of the targeted sensors. Our data show NADPH production in the mitochondria prior to the cytoplasm, nucleus, and peroxisome. The glucose-stimulated responses were also blocked by pyruvate transport inhibitor consistent with mitochondrial metabolism determining NADPH generation in the other organelles. Overall, we developed multiple organelle-targeted Apollo-NADP$^+$ sensors and revealed the dominance of beta-cell mitochondria in controlling NADPH/NADP$^+$ redox state across organelles.

1. Introduction

NADPH/NADP$^+$ redox state provides electrons to biosynthetic reactions required for cell growth and proliferation, and to recharging antioxidants required for survival (Ying, 2008). NADPH/NADP$^+$ redox state is thought to be somewhat compartmentalized due to a lack of known NADPH or NADP$^+$ membrane transporters, and the existence of organelle-specific enzymes for NADP$^+$ biosynthesis and reduction (Tran et al., 2021; Ying, 2008). Significant

compartmentalization could create disparate impacts on organelle-specific anabolism and antioxidation.

Pancreatic beta-cells metabolically respond to glucose to stimulate insulin secretion. This response includes a rise in NADPH/NADP$^+$ ratio. Cytoplasmic NADPH is normally generated by glucose-6-dehydrogenase (G6PD) activity in the oxidative branch of the pentose phosphate pathway (PPP) (Stanton, 2012). However, pancreatic beta-cells show limited G6PD activity (Schuit, De Vos, et al., 1997b) and thus rely on NADPH regeneration by malic enzyme (ME) (M. J. MacDonald, 1995; Pongratz et al., 2007; Rydström, 2006) and/or cytoplasmic isocitrate dehydrogenase (IDH1) (Ronnebaum et al., 2006). These enzymes are supported by metabolic efflux from the mitochondria. In a metabolic route termed pyruvate cycling, beta-cells metabolize pyruvate almost equally through pyruvate dehydrogenase (PDH) and pyruvate carboxylase (PC) resulting in a cascade of anaplerosis (i.e., refilling of TCA cycle intermediates), citrate/isocitrate efflux to the cytoplasm, and NADPH production via IDH1 activity (Jensen et al., 2008; Ronnebaum et al., 2006). Mitochondria generate their own NADPH using NADP$^+$-dependent isocitrate dehydrogenase (IDH2) and nicotinamide nucleotide transhydrogenase (NNT) activity (Vogel et al., 1999) with previous work suggesting NNT dominates the glucose-stimulated response (Aston-Mourney et al., 2007; Fergusson et al., 2014; Freeman et al., 2006; Toye et al., 2005). The apparent link between glucose-stimulated anaplerosis and insulin secretion has led to the hypothesis that NADPH is an amplifying signal to insulin secretion (Lu et al., 2002; G. F. Zhang et al., 2021). Thus, we aimed to measure the metabolic routes of beta-cell glucose-stimulated NADPH production and the extent of redox crosstalk between organelles.

Two genetically encoded NADH/NADP$^+$ redox state sensors are available including the NADPH-sensitive iNAP sensor (Moon et al., 2020; Tao et al., 2017) and the NADP$^+$-sensitive Apollo-NADP$^+$ sensors (Cameron et al., 2016). Apollo-NADP$^+$ sensors are based on NADP$^+$-induced dimerization of enzymatically inactive glucose-6-phosphate dehydrogenase (G6PD). Tagged with a single fluorescent protein, Apollo-NADP$^+$ sensors respond through changes in steady-state fluorescence anisotropy due to FRET between homologous fluorescent proteins (i.e., homoFRET). Importantly, anisotropy sensors consume less spectral bandwidth than conventional ratiometric sensors and can be swapped to distinct colors (i.e., they are spectrally tuneable), both of which facilitate multiparameter imaging (Cameron et al., 2016; Ross et al., 2018; Warren et al., 2015). In this study, we target Apollo-NADP$^+$ to various organelle compartments by first selecting for the most pH-stable fluorescent protein. We subsequently use simultaneous two-colour imaging to show a dominant role of mitochondrial NADPH generation in setting the glucose-stimulated responses in the cytoplasm, nucleus, and peroxisome.

2. Results

2.1. Determining pH sensitivity of Apollo-NADP$^+$. Fluorescent proteins are variably sensitive to pH, which could result in potential artifacts in the application of genetically encoded sensors. To select a fluorescent protein for Apollo-NADP$^+$ targeting, we first measured the impact of pH on the steady-state fluorescence anisotropy of a wide range of fluorescent protein tandem-dimers (EGFP, mVenus, Cerulean, Cerulean3, and mTurquoise2) (**Fig. 1a-b**). These tandem-dimers are connected by a short linker to ensure FRET between the homologous fluorescent proteins (homoFRET) (Ming et al., 2012; Regeenes et al., 2018), thus mimicking the low anisotropy of dimeric Apollo-NADP$^+$ (**Fig. 1a**). These data show a consistently low anisotropy in the blue

fluorescent protein tandem-dimers (Cer1, Cer3, mTurq2) across the full range of pH (**Fig. 1b**). In contrast, the EGFP and mVenus tandem dimers showed a progressive increase in anisotropy below pH 6.0. These data are consistent with the lower pKa values of the bluer fluorescent proteins (3.7 to 4.7) compared to EGFP and mVenus (6.0 and 5.5, respectively). Dropping pH below the pKa results in a fractional "darkening" of the fluorophore and an artifactual rise in anisotropy.

To further select from the blue fluorescent proteins, we compared the responses of Cer1-, Cer3-, and mTurq2-tagged Apollo-$NADP^+$ in response to NADPH oxidation by diamide (**Fig. 1c-d**). $NADP^+$-induced dimerization of Apollo-$NADP^+$ decreases the steady-state fluorescence anisotropy due to homoFRET (**Fig. 1c**). The blue sensors all showed responses to diamide treatment compared to monomeric control (R198I) and sensor in cells treated in normal media, with the largest statistically significant and dynamic responses found in cells expressing mTurq2-Apollo-$NADP^+$ (**Fig. 1d**). We were concerned pH could also impact $NADP^+$-induced dimerization of the catalytically inactive G6PD-backbone. To determine the impact of pH on sensor dimerization, we next compared the fluorescence anisotropy of Apollo-$NADP^+$ (mTurq2-Apollo-$NADP^+$) and R198I in cells treated with diamide (**Fig. 1e**). These data show stable sensor dimerization across a wide range of pH, with increased anisotropy found below pH 5.0. The ability of the sensor to dimerize in low pH is perhaps not surprising due to evidence that cytoplasmic G6PD translocates to the peroxisome and thus evolved to withstand variations in pH (Antonenkov, 1989; Frederiks et al., 2007; Patel et al., 1987). Overall, these data show mTurq2-Apollo-$NADP^+$ was the most dynamic of the pH stable sensors, and thus was chosen for subsequent organelle targeting.

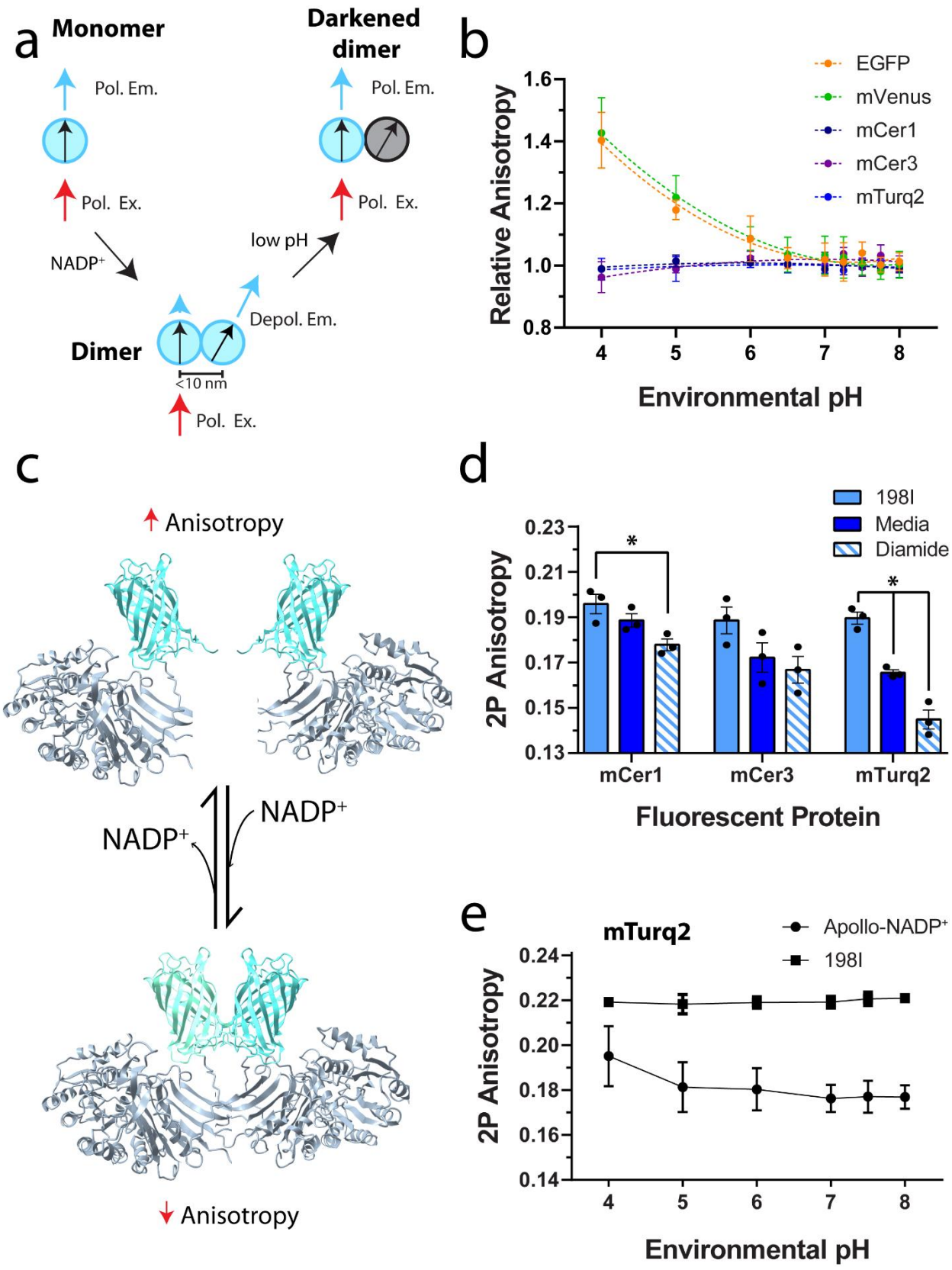
a
Monomer
Darkened dimer
Pol. Em.
Pol. Em.
Pol. Ex.
Pol. Ex.
NADP+
low pH
Depol. Em.
Dimer
<10 nm
Pol. Ex.
b
EGFP
mVenus
mCer1
mCer3
mTurq2
Relative Anisotropy
Environmental pH
c
Anisotropy
NADP+
NADP+
Anisotropy
d
198I
Media
Diamide
2P Anisotropy
mCer1
mCer3
mTurq2
Fluorescent Protein
e
mTurq2
Apollo-NADP+
198I
2P Anisotropy
Environmental pH

104

Figure 1. pH optimization of Apollo-NADP$^+$. (a) Exciting fluorescent proteins with polarized light results in relatively polarized emission and high steady-state fluorescence anisotropy (Monomer). FRET between homologous fluorescent proteins (homoFRET) occurs when the proteins are within ~10 nm resulting in depolarization of the emitted fluorescence and a corresponding drop in steady-state anisotropy (Dimer). A drop in pH below the fluorescent protein pKa would result in a fractional decrease in molecular brightness (Darkened dimer) along with an increase in apparent anisotropy. **(b)** Tandem-dimers of EGFP, mVenus, mCerulean (mCer1), mCerulean3 (mCer3), and mTurquoise2 (mTurq2) were expressed in AD293 cells and imaged under varying pH. Intracellular pH was controlled by equilibration with the extracellular buffer using 10 µM valinomycin and 10 µM nigericin. **(c)** The Apollo-NADP$^+$ sensor, comprised of enzymatically inactivated human G6PD tagged with fluorescent protein, responds to NADP$^+$ through allosteric dimerization. The cartoon structures are based on the crystal structures of human G6PD (PDB 6E07) and yellow fluorescent proteins (PDB 3V3D). **(d)** Apollo-NADP$^+$ and R198P-G6PD (R198I) tagged with mCer1, mCer3 and mTurq2 were imaged in AD293 cells in media. The Apollo-NADP$^+$ cells were subsequently imaged after treatment with diamide (5 min, 5 mM). Data represents mean ± S.E.M. for n = 3 independent trials. The * denotes significance <0.05 by 2-way ANOVA followed by a Tukey's multiple comparisons test. p-values are as follows from left to right: Cer1 (0.0217), mTurq2 (0.003 – 198I vs media, 0.0001 – 198I vs diamide, 0.0065 – media vs diamide). **(e)** Cells expressing the mTurq2 versions of Apollo-NADP$^+$ and R198I were exposed to 5mM diamide and imaged under varying pH. Data for all figures are mean ± S.E.M for n = 3 independent trials.

2.2. Organelle targeting of mTurq2-Apollo-NADP$^+$. We modified the mTurq2-Apollo-NADP$^+$ construct to express targeting sequences for the mitochondrial matrix, nucleus, ER lumen, plasma membrane, and peroxisome. To confirm successful organelle targeting, we imaged each sensor in AD293 cells (**Fig. 2a**). These images show localization and morphology consistent for each organelle (Goedhart, Von Stetten, et al., 2012). To validate the activity of the sensors in each organelle, we imaged a corresponding set of targeted controls (blue) and sensor in INS-1E beta-cells in response to glucose (0, 1, and 15 mM; red) and hydrogen peroxide (0.1, 10, and 1000 µM H_2O_2; yellow) **(Fig. 2b**). The controls included: (i) a similarly targeted full-length monomeric R198I, (ii) the sensor in cells treated with culture media, and (iii) sensor dimers induced by diamide. These controls defined the photophysical range of each sensor (i.e., monomer-to-dimer), except in the mitochondria and peroxisome where the R198I construct did not consistently target the organelle. The inability of the R198I construct to express in these organelles is consistent with an already destabilized construct being unable to fold/refold in these organelles (Cunningham et al., 2017). Notably, the anisotropies of the targeted R198I constructs were consistent across the other organelles (e.g., the cytoplasmic anisotropy was consistent with the nuclear anisotropy), and thus any of the other versions could serve as a monomeric control for the mitochondria and peroxisome. Based on these controls, sensor targeted to the cytoplasm, mitochondrial matrix, and nucleus showed consistent rises in anisotropy induced by glucose and falls in anisotropy induced by H_2O_2 that span a significant portion of the dynamic range (**Fig. 2b, top**). While the nuclear and cytoplasmic responses mirrored each other, the mitochondrial response to H_2O_2 was dampened, only showing a statistically significant response at 1000 µM H_2O_2. We postulate that this response was dampened by cytoplasmic H_2O_2-scavenging prior to reaching the organelle and by greater antioxidant capacity at high glucose. In contrast, ER-targeted sensor showed an elevated anisotropy with no response to any of these treatments including diamide (**Fig. 2b, bottom left**).

Consistent with non-functional sensor in the ER, INS-1E and AD293 cells also showed limited response to cortisone/hydrocortisone (data not shown), a treatment that affects ER NADPH/$NADP^+$ redox state via 11β-HSD-1 (Dzyakanchuk et al., 2009). Membrane-targeted sensor showed a statistically significant response to glucose; however, the sensor did not subsequently respond to H_2O_2 suggesting an irreversible/slow recovery of monomerization due to molecular crowding in 2D at the membrane surface (**Fig. 2b, bottom middle**). Finally, the peroxisomal sensor showed a significant response to high glucose, but a much smaller response to H_2O_2. The glucose response is consistent with the peroxisomes generating NADPH using G6PD and/or IDH1 activity (Antonenkov, 1989; Frederiks et al., 2007; Geisbrecht & Gould, 1999; Patel et al., 1987). The smaller H_2O_2 response is consistent with significant catalase activity in peroxisomes detoxifying H_2O_2 without consuming NADPH. Overall, these data show functional Apollo-$NADP^+$ sensors in the cytoplasm, nucleus, mitochondrial matrix, and peroxisome.

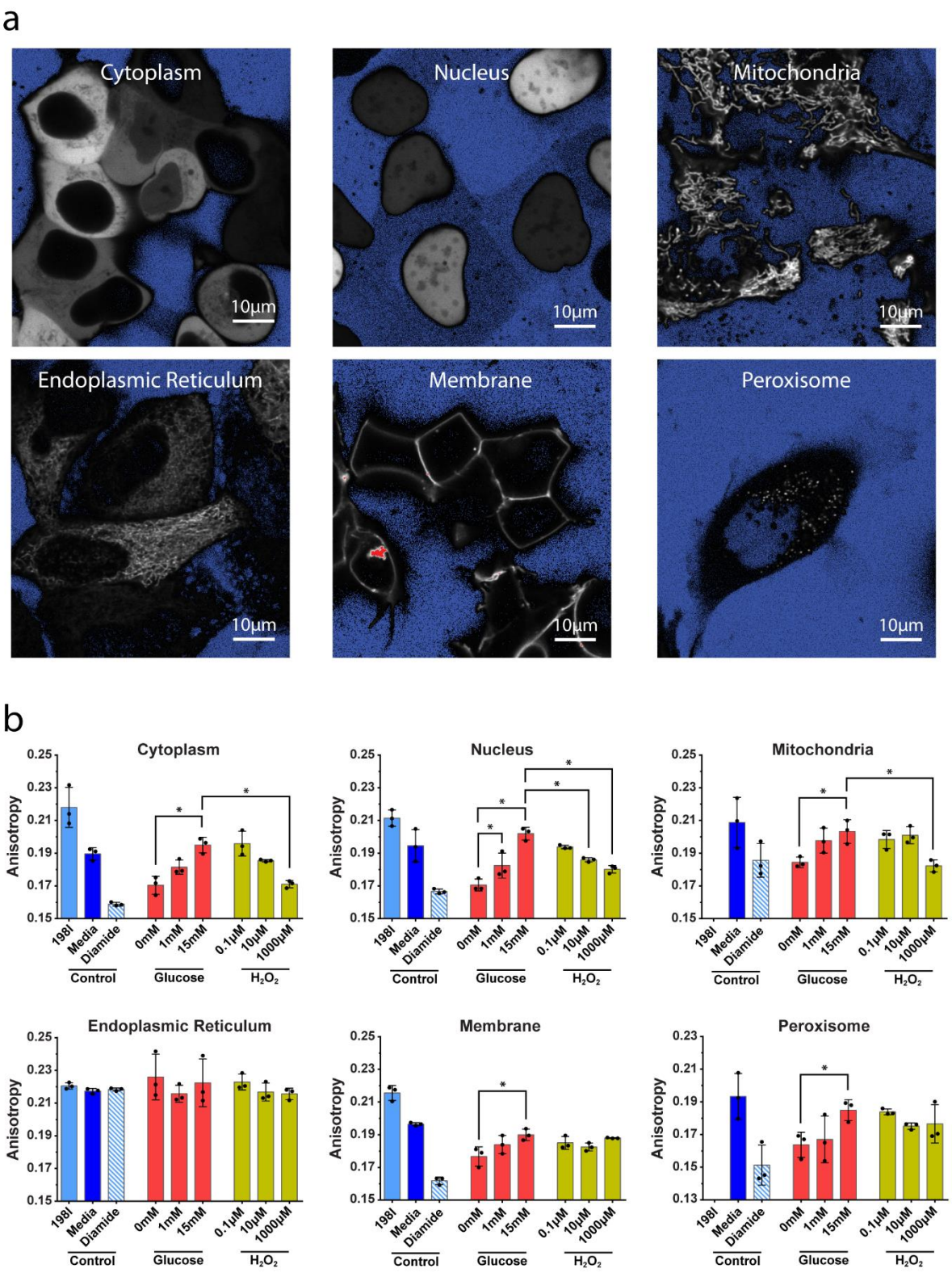

Figure 2. Characterization of organelle-targeted Apollo-NADP$^+$ constructs. (a) Representative images of mTurq2-Apollo-NADP$^+$ targeted to various subcellular compartments

and expressed in AD293 cells. **(b)** mTurq2-Apollo-$NADP^+$ and R198I constructs targeted to each organelle were expressed the INS-1E beta-cell line. Controls included the R198I monomeric control (198I, where expressed), the Apollo sensor in full media (media), and 5 mM diamide (diamide). Sensor expressing cells were imaged in sequential response to glucose (0, 1, and 15mM) and H_2O_2 (0.1, 10 and 1000 µM). Not shown are the R198I values for the mitochondria (0.178±.002) and the peroxisome (0.097±.002) as the low intensity of the images and the variance in anisotropy suggested these control constructs did not properly refold when targeted to these organelles. Data for all figures represent mean ± S.E.M. for n = 3 independent repeats. The * denotes significance <0.05 by 1-way ANOVA followed by a Tukey's multiple comparisons test. p-values are as follows from left to right: Cytoplasm (0.004, 0.005), Nucleus (0.03, <0.0001, 0.0036, 0.0002), Mitochondria (0.0148, 0.0068), Membrane (0.017), Peroxisome (0.042).

2.3. Imaging glucose- and glutamine-stimulated NADPH responses. In beta-cells pyruvate enters the TCA cycle nearly equally through PDH and PC, leading to a rise in TCA cycle intermediates (i.e., anaplerosis) and cytoplasmic NADPH generation due to mitochondrial citrate/isocitrate efflux (Cline et al., 2004; Khan et al., 1996; Lu et al., 2002; Michael J. MacDonald, 1993; Schuit, De Vos, et al., 1997a). To determine the metabolic route of glucose-stimulated NADPH production in beta-cells, we co-expressed cytoplasmic mVenus-Apollo-$NADP^+$ and mitochondrial mTurq2-Apollo-$NADP^+$ in INS-1E cells and simultaneously imaged the glucose-stimulated temporal responses (**Fig. 3a and 3b**). These data show NADPH generation plateaus in the mitochondrial matrix (~5 min, blue) prior to the cytoplasm (~9 min, yellow). Both responses were significantly diminished by the mitochondrial pyruvate transport inhibitor UK5099. Together, these data suggest glucose stimulates cytoplasmic NADPH production only after mitochondrial metabolism of pyruvate.

Glutamine also enters the TCA cycle anaplerotically through glutamate dehydrogenase (GDH) activity when triggered by the non-metabolizable leucine analogue BCH (G. F. Zhang et al., 2021). To confirm the role of anaplerosis in cytoplasmic NADPH generation, we measured the cytoplasmic and mitochondrial response to glutamine and BCH (**Fig. 3c**). These data show glutamine stimulates mitochondrial NADPH prior to the cytoplasm consistent with the cytoplasmic response depending on anaplerosis.

To further explore the role of mitochondrial metabolism, we simultaneously imaged the cytoplasmic and mitochondrial responses in cells treated with pyruvate transport inhibitor UK5099 and electron transport chain inhibitors (**Fig. 3d**). These data again show UK5099 abolishes the cytoplasmic and mitochondrial responses. The glucose-stimulated cytoplasmic and mitochondrial responses were also both blocked by collapse of the mitochondrial membrane potential (FCCP) and inhibition of the electron transport chain (rotenone). Collectively, these data suggest that both mitochondrial membrane potential and NADPH accumulation are required for a subsequent response in the cytoplasm. To measure the impact of anaplerosis on other organelles, we imaged glucose-stimulated responses in the nucleus and peroxisome in the presence of mitochondrial pyruvate transport inhibitor UK5099 (**Fig. 3e**). These data show UK5099 blocks responses in the nucleus and peroxisome. Overall, these data suggest mitochondrial NADPH accumulation precedes cytoplasmic, nuclear, and peroxisomal NADPH generation consistent with anaplerosis-dependent citrate/isocitrate efflux.

To validate our findings in primary tissue, we imaged the glucose-stimulated response of dispersed mouse islet cells transduced with cytoplasmic mVenus-Apollo-NADP$^+$ (**Fig 3f**). As expected, the glucose-stimulated response was abolished by UK5099 confirming in primary beta-cells that cytoplasmic NADPH generation depends on mitochondrial pyruvate metabolism.

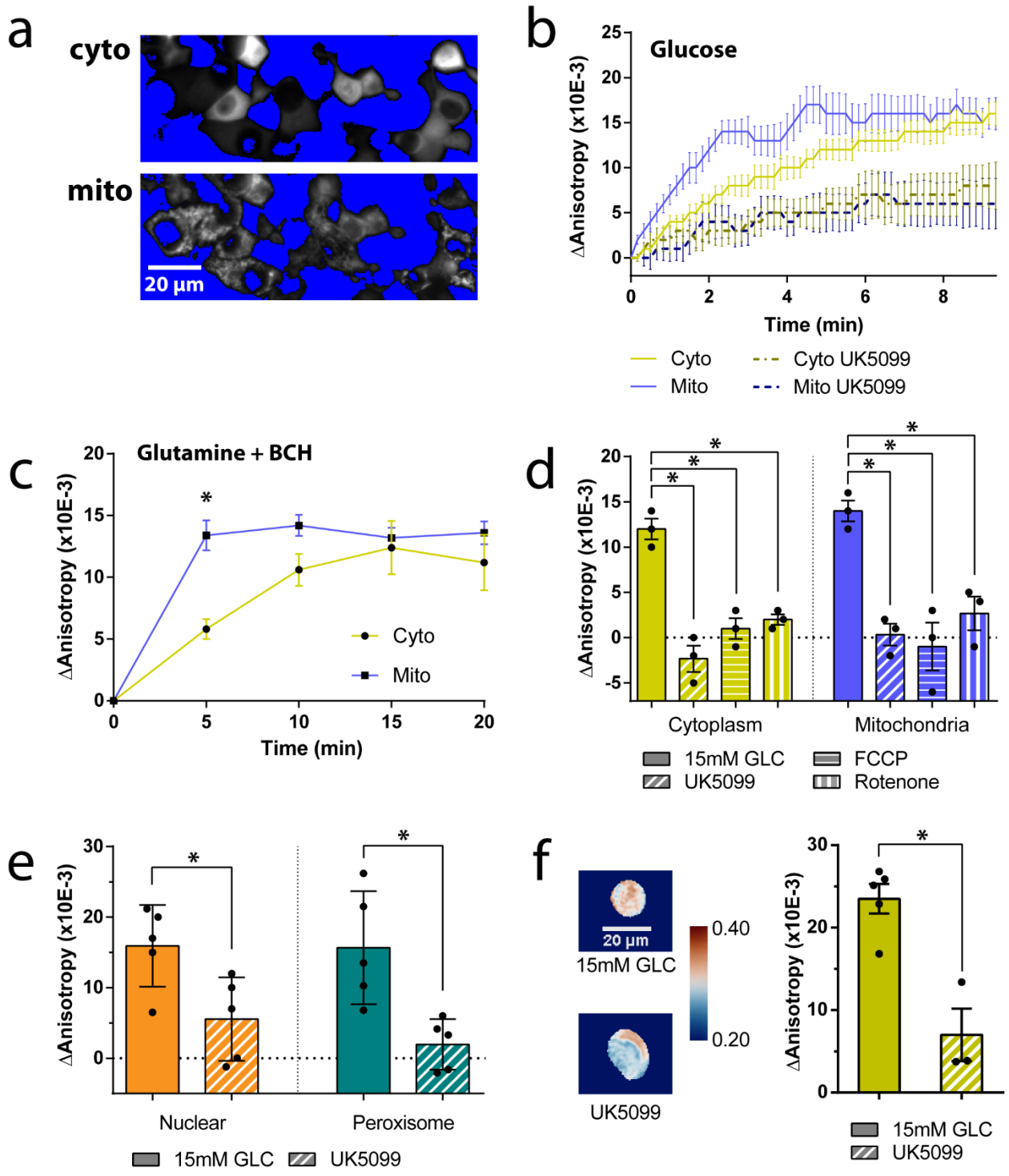

Figure 3. Determining the role of mitochondrial pyruvate transport and anaplerosis on cytoplasmic and mitochondrial NADPH. INS-1E cells were transfected to co-express mVenus cytoplasmic-Apollo-NADP$^+$ (Cyto) and mTurq2 mitochondrial-Apollo-NADP$^+$ (Mito). **(a)** Representative images of the sensors with similar thresholding and a 1 pixel median filter applied to remove background noise. **(b)** The temporal response to 15 mM glucose bolus was compared to cells pre-treated for 1 hr with 50 µM UK5099. The cytoplasmic and mitochondrial sensors were imaged from each field of view at a frequency of 6 images/min. Data are reported as the mean change in anisotropy (ΔAnisotropy ($\times 10^{-3}$)) ± S.E.M. for n = 5 repeats with at least 5 cells (replicates) per repeat. **(c)** The temporal response to a 10 mM BCH bolus was imaged in cells also pre-treated for 1 hr in 5 mM glutamine. Images were collected from multiple fields of view every 5 min. Data are reported as the mean change in anisotropy (ΔAnisotropy ($\times 10^{-3}$)) ± S.E.M. for n = 3 repeats with ~30 cells (replicates) per repeat. The * denotes significance by row-repeated measures (time) 2-way ANOVA, followed by a Sidak's multiple comparisons test. p-value = 0.0006. **(d)** The anisotropy changes after 5 min of glucose bolus (1 to 15 mM) comparing control cells to cells pre-treated with UK5099 (50 µM, 1 hr), FCCP (1 µM, 5 min) and rotenone (1 µM, 5 min). The * denotes significance by 2-way ANOVA followed by a Dunnett's multiple comparisons test. Cytoplasmic p-values = <0.0001 (glucose vs. UK5099), 0.0003 (glucose vs. FCCP), 0.0007 (glucose vs. rotenone), respectively. Mitochondrial p-values = <0.0001 (glucose vs. UK5099), <0.0001 (glucose vs. FCCP), 0.0002 (glucose vs. rotenone), respectively. **(e)** Cells expressing nuclear or peroxisomal mTurq2-tagged sensor were starved in 1mM glucose and 50 µM UK5099 for 1hr, then treated with glucose (15mM) for 10 min (nuclear) or 20 min (peroxisome), respectively. Data represents mean ± S.E.M. for n = 5 repeats with 15-25 cells (replicates) per repeat. The * denotes significance by paired t-test. p-values = 0.0291 (nuclear) and 0.0235 (peroxisome), respectively. **(f)** Mouse islets were dispersed to single cells and transduced with cytoplasmic Apollo-NADP$^+$. (**f- left**) Representative anisotropy images of cells from the dispersed mouse islets. The images were similarly thresholded and a 1 pixel median filter was applied to remove background noise. Both cells were treated with 15 mM glucose (5 min) while the bottom cell was also pretreated with UK5099 (50 µM, 1 hr). Colour map is *vik* from an array of scientific colour maps developed by Fabio Crameri (Crameri, 2018). **(f – right)** Cytoplasmic anisotropy responses of dispersed mouse islets to a 15 mM glucose bolus (15 min) in control cells (15 mM GLC) or cells pre-treated with UK5099 (50 µM, 1 hr). Data are reported as the mean change in anisotropy (ΔAnisotropy ($\times 10^{-3}$)) ± S.E.M. for n = 3-5 repeats with at least 15 cells (replicates) per repeat. Control replicates are shared with **Fig. 4f** since the data was collected at the same time. The * denotes significance by 1-way ANOVA followed by a Tukey's multiple comparison test. p-value = 0.0134.

Imaging the impact of fatty acids on the glucose-stimulated NADPH response. Fatty acids enter the TCA cycle catabolically and thus do not stimulate significant NADPH production in beta-cells (data not shown). Fatty acids will however impact glucose-stimulated NADPH production through inhibition of PDH activity by acetyl-CoA (Batenburg & Olson, 1976), and through inhibition of NNT activity at higher chain lengths (Rydström, 1972) (**Fig. 4a**). Octanoate freely diffuses into the mitochondrial matrix without requiring transport by carnitine palmitoyltransferases resulting in beta-oxidation to acetyl-CoA. To measure the impact of octanoate on glucose-stimulate NADPH responses, we co-expressed cytoplasmic (mVenus) and mitochondrial (mTurq2) sensors to simultaneously image each organelle response (**Fig. 4b-c**). These data presented in a scatter plot (**Fig. 4b**) and bar graph (**Fig. 4c**) show octanoate pre-treatment decreases the glucose-stimulated cytoplasmic response with minimal impact on the

mitochondrial response. Consistent with inactivation of PDH, DCA restored the cytoplasmic response while leaving the mitochondrial response unaffected. Since pyruvate-derived anaplerosis depends on both PC and PDH activity, these data are consistent with octanoate blocking the cytoplasmic NADPH response by reducing anaplerosis.

To determine the role of NNT in the glucose-stimulated mitochondrial NADPH response, we next pretreated cells with palmitate, a longer chain fatty acid well-established to inhibit NNT activity (**Fig. 4d-e**) (Rydström, 1972). These data presented in a scatter plot (**Fig. 4d**) and bar graph (**Fig. 4e**) show palmitate abolished both the cytoplasmic and mitochondrial glucose-stimulated responses consistent with inhibition of both PDH (via acetyl-CoA) and NNT (via palmitoyl-CoA). In contrast to octanoate, the cytoplasmic response in the presence of palmitate was not recovered by DCA. Thus, we postulate that the cytoplasmic response depends on both mitochondrial anaplerosis and NNT activity.

To validate these findings in primary tissue, we imaged the impact of octanoate pre-treatment on the glucose-stimulated response of dispersed mouse islet cells transduced with cytoplasmic mVenus-Apollo-$NADP^+$ (**Fig. 4f**). Pre-treating dispersed islets with octanoate significantly diminished the glucose-stimulated NADPH response and this response was fully restored by activation of PDH using DCA. These data are again consistent with the cytoplasmic NADPH response being dependent on mitochondrial anaplerosis in primary cells.

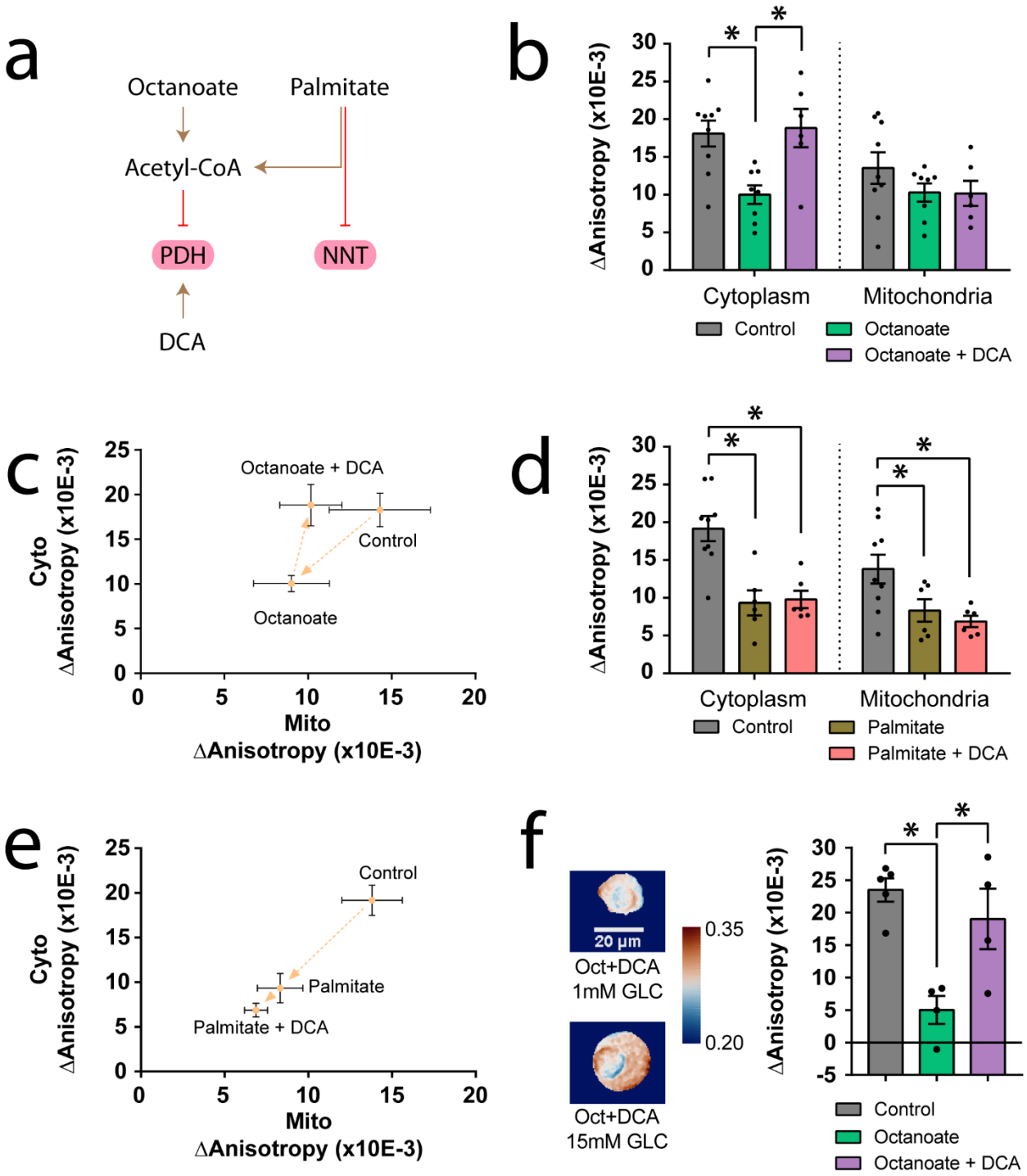

Figure 4. Determining the roles of non-anaplerotic fatty acids and NNT activity on cytoplasmic and mitochondrial NADPH. (a) A schematic showing the anticipated impact of octanoate and palmitate on PDH and NNT activity. Acetyl-CoA produced by beta-oxidation of both fatty acids will inhibit PDH activity with DCA reversing this effect. Longer chain fatty acid palmitate is also a direct inhibitor of NNT. **(b-e)** INS-1E cells co-expressing cytoplasmic (mVenus) and mitochondrial (mTurq2) Apollo-NADP$^+$ were incubated in 1 mM glucose plus pre-treatments as indicated prior to imaging. **(b)** Cytoplasmic and mitochondrial anisotropy responses

to a 15 mM glucose bolus (15 min) were simultaneously imaged in cells pre-treated with 400 µM octanoate (30 min), 400 µM octanoate and 1 µM DCA (30min), or no treatment (control). Data are reported as the mean change in anisotropy (ΔAnisotropy ($\times 10^{-3}$)) ± S.E.M. for n = 6-9 independent repeats with at least 15 cells (replicates) per repeat. The * denotes significance by 2-way ANOVA followed by a Tukey's multiple comparisons test. p-values = 0.0043 (control vs. octanoate) and 0.0052 (octanoate vs. octanoate + DCA), respectively. **(c)** The same anisotropy changes from (b) shown in scatter plot. Dotted arrows denote the order they are described in the results. **(d)** Cytoplasmic and mitochondrial anisotropy responses to a 15 mM glucose bolus (15 min) were simultaneously imaged in cells pre-treated with 400 µM palmitate only (4 hr), 400 µM palmitate (4 hr) followed by 1 µM DCA (30 min), or no treatment (control). Data are reported as the mean change in anisotropy (ΔAnisotropy ($\times 10^{-3}$)) ± S.E.M. for n = 5-9 independent trials with at least 10 cells (technical replicates) per trial. The * denotes significance by 2-way ANOVA followed by a Dunnett's multiple comparisons test. Cytoplasmic p-values = 0.0002 (control vs. palmitate) and 0.0004 (control vs. palmitate + DCA), respectively. Mitochondrial p-values = 0.0417 (control vs. palmitate) and 0.0086 (control vs. palmitate + DCA), respectively. **(e)** The same anisotropy changes from (d) shown in scatter plot. Dotted arrows denote the order they are described in the results. **(f)** Mouse islets were dispersed to single cells and transduced with cytoplasmic Apollo-NADP$^+$. **(f – left)** Representative anisotropy images of dispersed mouse islets similarly thresholded and filtered using a 1 pixel median filter to remove background noise. Images show islet cells stimulated with 15 mM (15 min) after pre-treatment in 400 µM octanoate (30min, top) and 400 µM octanoate + 1 µM DCA (30min, bottom). Colour map is *vik* from an array of scientific colour maps developed by Fabio Crameri (Crameri, 2018). **(f – right)** The glucose-stimulated (15 mM, 15 min) anisotropy responses of dispersed mouse islet cells (control) compared to response of cells pre-treated with 400 µM octanoate (30 min) and 400 µM octanoate + 1 µM DCA (30 min). Data are reported as the mean change in anisotropy (ΔAnisotropy ($\times 10^{-3}$)) ± S.E.M. for n = 4-5 repeats with at least 15 cells (replicates) per repeat. Control replicates are shared with **Fig. 3f** since the data was collected at the same time. The * denotes significance by 1-way ANOVA followed by a Tukey's multiple comparisons test. p-values = 0.0033 (control vs. octanoate) and 0.0300 (octanoate vs. octanoate + DCA), respectively.

3. Discussion

Our goal was to target Apollo-NADP$^+$ to various organelles to measure NADPH generation and compartmentalization in beta-cells. Taking advantage of the tuneability of Apollo-sensors, we first measured the impact of pH on the apparent anisotropy. These studies led us to target mTurq2-Apollo-NADP$^+$ as the most dynamic, pH-stable sensor (Goedhart, Stetten, et al., 2012). We subsequently confirmed sensor activity in the cytoplasm, mitochondrial matrix, nucleus, and peroxisome by imaging responses to glucose and H_2O_2-scavenging. We applied these sensors in both single and dual colour imaging, showing mitochondria are 'master regulators' of beta-cell NADPH production across all the other organelles. Overall, this work expands the Apollo-NADP$^+$ family of sensors while revealing a dominant role of mitochondrial metabolism in setting beta-cell NADPH/NADP$^+$ redox state across organelles.

In contrast to the cytoplasm (Orij et al., 2009), ER (Wu et al., 2000) and nucleus (Llopis et al., 1998), the mitochondrial matrix (Poburko et al., 2011) and peroxisome (Jankowski et al., 2001)

can show significant variability in physiological pH. This variability complicates the application of genetically encoded sensors in these organelles. Although some pH sensitivity is not insurmountable, the methods to correct for it (e.g., co-expressing a pH sensor or an inactivated sensor) (Moon et al., 2020; Orij et al., 2009) work against the ability to track single cells and to perform multiparametric imaging. Since Apollo-NADP$^+$ sensors are based on a single colour, we were able to overcome this limitation by swapping in different fluorescent proteins. In general, the bluer fluorescent protein dimers (mCer, mCer3, and mTurq2) were more pH-stable than the greener fluorescent protein dimers (mVen, EGFP) likely due to lower pKa (pKa~3.2) (Lambert, 2019). We subsequently settled upon the mTurq2 version as the most dynamic sensor noting the sensor responses tracked well with the quantum yield (QY) of each fluorescent protein (mTurq2 (0.93) > mCer3 (0.87) >> mCer(0.49)) (Lambert, 2019). This trend is consistent with the single fluorescent protein acting as both donor to impact Förster distance ($R_0 \propto (QY_D)^{½}$) and acceptor to impact the energy transmitted as depolarized fluorescence ($I_A \propto QY_A$). Thus, we settled on targeting the mTurq2 version of the sensor due to having the highest pH stability and apparent dynamic range.

We proceeded with dual colour imaging of organelle-targeted mTurq2-Apollo-NADP$^+$ sensors to examine beta-cell NADPH production. It is well established that beta-cells sense glucose through the low-affinity high-capacity hexokinase glucokinase (Matschinsky et al., 1993) and a subsequent rise in ATP:ADP ratio that triggers closure of ATP-sensitive potassium (K_{ATP}) channels. This cascade of membrane depolarization leads to Ca^{2+} influx through voltage-gated channels and insulin secretion (Newgard & McGarry, 1995). Notably, auxiliary metabolic routes that siphon glycolytic intermediates, such as the PPP (Lee et al., 2011; Michael J. MacDonald, 1993; Pullen et al., 2014; Schuit, Vos, et al., 1997; Z. Zhang et al., 2010) and lactate efflux (Pullen et al., 2014), are turned off in beta-cells to ensure a tight link between glucose stimulation and insulin secretion. Thus, our metabolic model incorporates pyruvate cycling as the primary source of cytoplasmic NADPH (**Fig. 5**). Pyruvate cycling is initiated in beta-cells by nearly equal entry into the TCA cycle through PDH and PC. This dual entry results in anaplerosis, triggering mitochondrial citrate/isocitrate efflux and subsequent production of cytoplasmic NADPH via ME and/or IDH1. Consistently, we showed NADPH production in the mitochondria preceded that of the cytoplasm, with both responses blocked by the pyruvate transport inhibitor UK5099. An alternative source of anaplerosis, glutamine, also stimulated mitochondrial NADPH production before the cytoplasm.

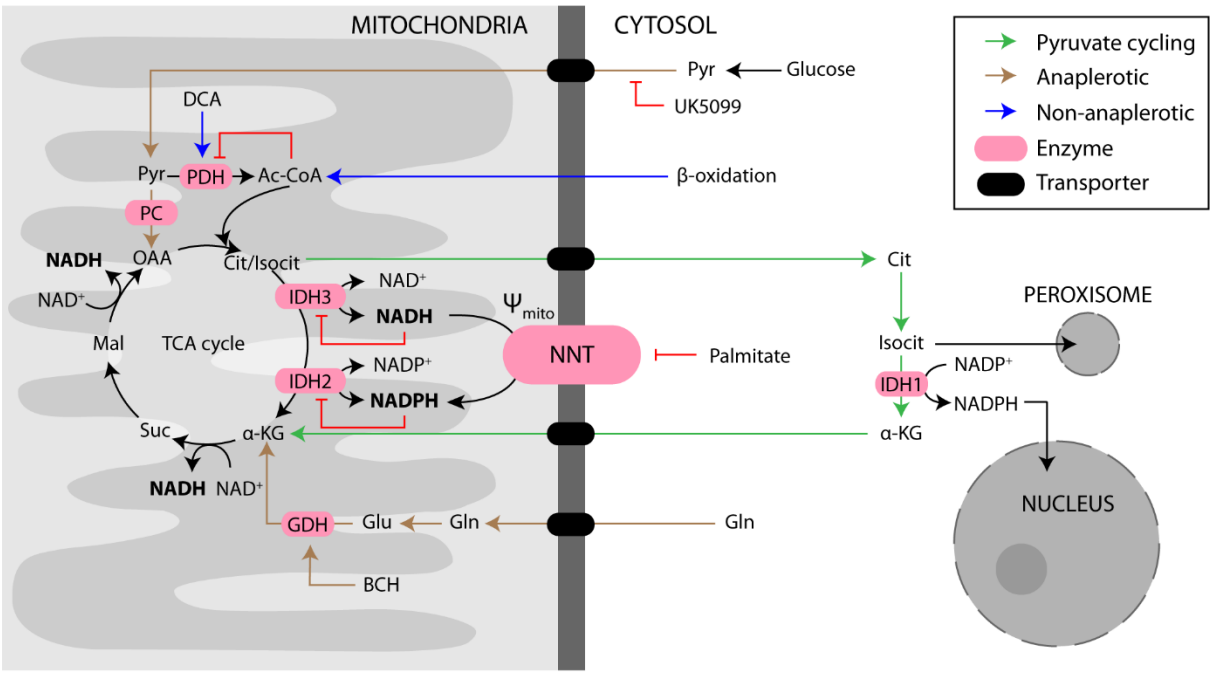

Figure 5. Proposed model of beta-cell NADPH generation in the mitochondria, cytosol, nucleus, and peroxisome. Glucose metabolized to pyruvate by glycolysis enters the mitochondria though the pyruvate transporter, which can be inhibited by UK5099. Pyruvate enters the TCA cycle through both pyruvate dehydrogenase (PDH, catabolism) and pyruvate carboxylase (PC, anaplerosis) activity resulting in a buildup of TCA cycle intermediates. Mitochondrial efflux of citrate/isocitrate results in cytoplasmic NADPH generation via IDH1 activity as well as completion of the "pyruvate-cycle" by entry of alpha-ketoglutarate back into the TCA cycle. The model includes spillover of isocitrate to the peroxisome and NADPH diffusion into the nucleus to account for a rise in NADPH in those organelles. Glutamine also enters the TCA cycle by anaplerosis via glutamate dehydrogenase when activated by BCH. Beta-oxidation of fatty acids produces acetyl-CoA, which inhibits PDH activity. This inhibition can be reversed in the presence of DCA, which activates pyruvate dehydrogenase. Mitochondrial NADH generation fuels the NNT, which converts NADH to NADPH when mitochondrial membrane potential is high. The long chain fatty acid palmitate inhibits NNT activity. Our data are consistent with NADPH generated by NNT inhibiting/reversing IDH2/3 activity, which may be a prerequisite for citrate/isocitrate accumulation, efflux, and subsequent cytoplasmic NADPH generation. **Abbreviations:** Pyruvate (Pyr), Acetyl-CoA (Ac-CoA), pyruvate dehydrogenase (PDH), pyruvate carboxylase (PC), $NADP^+$-dependent cytoplasmic isocitrate dehydrogenase (IDH1), $NADP^+$-dependent mitochondrial isocitrate dehydrogenase (IDH2), NAD^+-dependent mitochondrial isocitrate dehydrogenase (IDH3), glutamate dehydrogenase (GDH), oxaloacetate (OAA), citrate (Cit), Isocitrate (Isocit), alpha-ketoglutarate (α-KG), succinate (Suc), malate (Mal), glutamine (Gln), glutamate (Glu), nicotinamide nucleotide transhydrogenase (NNT).

To further examine the role of anaplerosis in cytoplasmic NADPH generation, we measured the impact of catabolic fatty acids on the glucose-stimulated mitochondrial and cytoplasmic responses.

We postulated that inhibition of PDH by acetyl-CoA would lessen cytoplasmic NADPH response by decreasing metabolic flux through citrate synthase and/or increasing isocitrate consumption by NAD^+-dependent isocitrate dehydrogenase (IDH3) (**Fig. 5**). Consistently, blocking PDH through the short chain fatty acid octanoate inhibited cytoplasmic, but not mitochondrial, NADPH generation. Additionally, the PDH activator DCA rescued the cytoplasmic response.

Finally, our data and previous work suggest that NNT dominates glucose-stimulated mitochondrial NADPH production leading to inhibition/reversal of IDH2 activity (**Fig. 5**) (Rydström, 2006; Smolková & Ježek, 2012; Vogel et al., 1999). Consistent with this model, the glucose-stimulated cytoplasmic and mitochondrial NADPH responses were abolished by inhibiting NNT using palmitate and by blocking mitochondrial membrane potential (FCCP, rotenone). Thus, we postulate that the inhibition of IDH2/3 by mitochondrial NADPH may be a prerequisite for isocitrate/citrate accumulation and efflux, and ultimately determine cytoplasmic NADPH production. This model uniquely highlights the interaction between NNT and IDH2/3 through mitochondrial NADPH to proportionally link mitochondrial activity to cytoplasmic NADPH production.

The glucose-stimulated nuclear and peroxisomal responses were also blocked by UK5099. Notably, the nuclear response mirrored the cytoplasmic response consistent with previous work suggesting NADPH is readily diffusible between cytoplasmic and nuclear compartments (**Fig. 5**) (Moon et al., 2020). Thus, the nuclear targeted sensor could potentially serve as a useful surrogate for the cytoplasmic sensor to improve spatial separation during multiparameter imaging and to better isolate individual cell responses in tissues. However, substitution of the nuclear sensor will need to be fully considered in the context of varied compartmentalization of glutathione in the nucleus during the cell cycle (Bellomo et al., 1992; Pallardó et al., 2009; Tao et al., 2017). The peroxisome normally maintains $NADPH/NADP^+$ redox state through translocation of cytoplasmic G6PD (Antonenkov, 1989; Frederiks et al., 2007; Patel et al., 1987) and IDH1 (Geisbrecht & Gould, 1999). Thus, our data are consistent with low G6PD activity in beta-cells leaving the peroxisome also dependent on mitochondrial efflux and NADPH production by IDH1 alone (**Fig. 5)**. We therefore speculate that NADPH in beta-cell peroxisomes could become limited particularly during mitochondrial dysfunction to impact ROS scavenging during the beta-oxidation of long-chain fatty acids (Minard & McAlister-Henn, 1999) and the biosynthesis of ether phospholipids plasmalogens (Okumoto et al., 2020).

Beta-cell dysfunction is associated with the earliest stages of type 2 diabetes (T2D) and has been previously attributed to chronic oxidative stress associated with insulin secretion combined with limited antioxidant enzyme activity (Tiedge et al., 1997). We postulate that a reliance on pyruvate cycling as an alternative to G6PD/PPP leaves beta-cells vulnerable to the oxidative stress. A new concern raised here is that a reliance on pyruvate cycling could also limit nuclear and peroxisomal NADPH production, impacting scavenging and biosynthetic reactions in these organelles. We therefore posit that mitochondrial dysfunction in the context of NADPH production should be considered a primary target for the treatment of T2D on top of a recognized role in producing and scavenging of ROS (Haythorne et al., 2019).

4. Materials and Methods

4.1. Key Resources Table

Reagent type (species) or resource	Designation	Source or reference	Identifiers	Additional information
Strain, strain background (C57BL/6, males)	C57BL/6		RRID: IMSR_JAX:000664	Jackson Laboratory, Bar Harbor, ME, USA
Genetic reagent	pcDNA 3.1	ThermoFisher Scientific	#V79020	
Cell line	INS-1E	PMID: 14592952	RRID: CVCL_0351	University of Geneva, CH. Obtained from lab of Michael B. Wheeler
Cell line	AD293	Agilent	#240085	
Transfected construct	Cytoplasmic mVenus-Apollo-NADP$^+$	PMID: 26878383	Addgene Plasmid #71797	Lab of Dr. Jonathan Rocheleau
Transfected	Mitochondrial	This paper		Lab of Dr.

construct	mTurq2-Apollo-NADP$^+$			Jonathan Rocheleau
Transfected construct	Cytoplasmic mTurq2-Apollo-NADP$^+$	This paper		Lab of Dr. Jonathan Rocheleau
Transfected construct	Nuclear mTurq2-Apollo-NADP$^+$	This paper		Lab of Dr. Jonathan Rocheleau
Transfected construct	Peroxisomal mTurq2-Apollo-NADP$^+$	This paper		Lab of Dr. Jonathan Rocheleau
Commercial assay or kit	PolyJet Transfection Reagent	FroggaBio	SL100688.1	
Commercial assay or kit	Lipofectamine 3000 Transfection Reagent	Life Technologies	L3000015	
Sequence-based reagent	pcDNA-MitoIns-FWD	ACCCAAGCTGGCTAGTCGTCAGATCCGCTAGCAT		Insertion of MTS

Sequence-based reagent	pcDNA-MitoIns-REV	GCTCGGTACCAAGCTTATCGAGCAACGAATGGATC		Insertion of MTS
Sequence-based reagent	pcDNA-NucIns-FWD	CAGTGTGGTGGAATTCATGgctccaaagaagaagcgtaaggtaGCAGAGCAGGTGGC		Insertion of SV40 T-antigen
Sequence-based reagent	pcDNA-NucIns-REV	taccttacgcttcttctttggagcCTTGTACAGCTCGTCC		Insertion of SV40 T-antigen
Sequence-based reagent	pcDN-FP-AgeI-Rcb-FWD	CACAAGCTCagAccggTCGCCACCATGGTGAGC		
Sequence-based reagent	pcDNA Perox-V2-XhoI-REV	GCCCTCTAGACTCGAGttataacttgctGCGGCGGCGCTTGTACAGCTCGTCCATGC		

4.2. Molecular biology of sensor targeting. We originally cloned Cerulean and mVenus-tagged Apollo-NADP$^+$ into the *NheI/XhoI* sites of pcDNA3.1 (--*NheI*—mutant G6PD--*AgeI*—Fluorescent protein--*XhoI*--). The mTurqoise2 and Cerulean3 versions of Apollo-NADP$^+$ were subsequently created by exchanging the fluorescent protein using the *AgeI/Xho1* sites. Organelle targeting sequences were subsequently introduced into the mTurquoise2 version of Apollo-NADP$^+$. These smaller tags were introduced using cloning primers: (i) the nuclear targeting sequence of SV40 T-antigen 'PKKKRK' was cloned into the N-terminus (Mahato et al., 1999), (ii) the peroxisome targeting sequence –SKL was cloned into the C-terminus (Gould et al., 1989), and (iii) the ER retention KDEL sequence was cloned into the C-terminus. Larger tags were cloned into the *NheI* and *BamHI/HindIII* sites, placing the targeting sequence on the N-terminus of Apollo-NADP$^+$ (--*NheI*—targeting sequence--*BamHI/HindIII*-mutG6PD--*AgeI*--FP--*XhoI*--). This included the mitochondrial matrix targeting sequence from pKillerRed-dMito (a gift from Peter Kim, SickKids Hospital, Toronto), which we cloned in twice to get four copies of the mitochondrial targeting sequence (4x MTS). Finally, the membrane targeting sequence of neuromodulin was cloned from pEYFP-Mem, and the ER targeting sequence of calreticulin was

cloned from pECFP-ER (Clonetech, San Jose, CA). All constructs were confirmed by sequencing. All plasmid amplification was performed using 5-alpha competent E. coli (NEB, Ipswich, MA, C2987I)

4.3. Cells and cell culture. INS-1E (obtained from lab of Michael B. Wheeler, RRID: CVCL_0351) and AD293 (Agilent, Santa Clara, CA, #240085) cells were cultured in RPMI and DMEM media, respectively under humidified 5% CO_2 at 37°C. For imaging, cells were plated into No 1.5 glass bottom dishes (MatTek Corporation, Ashland, MA) and transfected the next day (0.5-1.0 µg/dish/plasmid) using Poly-Jet reagent (for AD293s) (SignaGen, Frederick, MD) or Lipofectamine 3000 (for INS-1Es) (Invitrogen, Burlington, Canada) and incubated for 24 hr. The media was replaced with fresh media and the cells were left to recover for a further 24 hr prior to imaging.

4.4. Clamping the intracellular pH of live cells. Cytoplasmic pH was varied by incubating the target cells with buffers and equilibrating the intracellular and extracellular pH levels using 10 µM of valinomycin and 10 µM nigericin, as described previously (Loiselle & Casey, 2010).

4.5. Islet isolation, dispersion, and transduction. Animal procedures were approved by the Animal Care Committee of the University Health Network, Toronto ON, Canada, in accordance with the policies and guidelines of the Canadian Council on Animal Care (Animal Use Protocol number 1531). Pancreatic islets were isolated from 8- to 12-week-old C57Bl/6J (Jackson Lab, Bar Harbor, ME, RRID: IMSR_JAX:000664) male mice by collagenase digestion (Roche Applied Science) (Sun et al., 2012). Isolated islets were transferred into an Eppendorf tube (1.5 ml) containing 50 µl RPMI islet media and 50 µl Trypsin:EDTA solution. Tubes were immersed in a water bath at 37 °C and shaken gently by hand for 12 min. Once fully dissociated, the islet slurry was supplemented up to 1 ml total volume with RPMI islet media. Glass bottom plates (48-well) were incubated with a layer of Poly-D-Lysine (PDL) hydrobromide (Sigma-Aldrich, Product #P6407) for 1 h at 37°C to promote dispersed islet cell adhesion. The dispersed cells were transduced with adenovirus (24 hr at 1:10 dilution or ~ 2×10^7 IFU/ml) (Pal et al., 2022) (manuscript accepted). Viral titers were measured using the Adeno-X rapid titer kit (Clontech) following the manufacturer's protocol.

4.6. Cellular imaging. All imaging was done in BMHH imaging buffer (125 mM NaCl, 5.7 mM KCl, 2.5 mM $CaCl_2$, 1.2 mM $MgCl_2$, 0.1% BSA, and 10 mM HEPES at pH 7.4). Single colour two-photon fluorescence anisotropy imaging was performed using an LSM710 confocal microscope (Zeiss, Toronto, Canada) equipped with a tunable Chameleon laser (Coherent, Santa Clara, CA). Images were collected using 840 nm (Cerulean) or 950 nm (Venus) excitation and a 63×/1.4–numerical aperture (NA) oil-immersion objective. Fluorescence was collected using the non-descanned binary GaAsP BiG (Zeiss, Toronto, Canada) detector with a custom-built filter cube containing an infrared light–blocked Cerulean (ET480/40M-2P) or Venus (ET525/50M-2P) emission bandpass filter (Chroma, Bellows Falls, VT), polarizing beam-splitter (Edmund Optics, Barrington, NJ) and clean-up polarizers (Chroma, Bellows Falls, VT). Channels 1 and 2 simultaneously collected the perpendicular and parallel emission. Simultaneous two-colour fluorescence anisotropy imaging was performed using a custom-built widefield RAMM microscope (ASI) equipped with excitation LEDs (405, 505, and 590nm), and excitation polarizing filter (Edmund Optics, Barrington, NJ). Images were collected using a 60×/1.42 NA oil-immersion or a 40×/0.75 NA air objective lens (Olympus, Richmond Hill, Canada). Fluorescence was passed

through either a Cerulean (ET470/24M) or Venus (ET535/30M) emission filter on a filter wheel, and subsequently split using an Optosplit II (Cairn, Faversham, UK) to simultaneously collect parallel and perpendicular emission light on separate regions of an IRIS 15 CMOS camera (Teledyne Photometrics, Tucson, AZ).

4.7. Image analysis. Parallel ($I_{\parallel}$) and perpendicular ($I_{\perp}$) fluorescence intensity images were analyzed with a custom ImageJ plugin (available at https://github.com/RocheleauLab/Optosplit-Anisotropy-Analysis-scripts). The images were first background corrected using a rolling ball filter. Pixel-by-pixel anisotropy (r) was subsequently calculated using the background corrected intensities: $r = (I_{\parallel} - GI_{\perp})/(I_{\parallel} + 2G_{\perp})$ (Axelrod, 1979). The G factor correction accounts for differences in the equipment to detect parallel and perpendicular light. The G factor for our point-scanning two-photon microscope was measured by exciting samples with both vertically (V) polarized and horizontally (H) polarized light and collecting the polarized emission (V and H) (Blackman et al., 1996; Rocheleau et al., 2003). The G-factor for our widefield microscope was calculated using fluorescein solutions that have a near zero steady-state fluorescence anisotropy, thus simplifying the standard anisotropy equation to measure $G = I_{\parallel} / I_{\perp}$. For images collected using the 1.42 NA objective lens, we used additional correction factors (K_a, K_b, and K_c) to account for the blurring of parallel and perpendicular intensities (Axelrod, 1979). Regions of interest (ROI) were selected using the parallel or perpendicular intensity images, instead of the anisotropy image, to avoid selection bias.

4.8. Statistics. All data are presented as mean ± S.E.M based on at least three separate experiment days. Iglewicz and Hoaglin's robust test for multiple outliers was used to detect and remove outliers from technical replicates. Statistical significance was determined using Prism 6 (GraphPad, San Diego, CA). Specific statistical tests are listed where appropriate in each corresponding figure legend, but as a general statement, post-hoc tests were used to determine significance between groups following ANOVA. Tukey's multiple comparison tests were used when making comparisons between all groups. Dunnett's multiple comparison tests were used when making comparions between the control group vs other groups only. Anisotropy measurements were confirmed as normally distributed using a normal probability plot and D'Agostino-Pearson normality tests. The variance of the anisotropy values was consistent within samples and across experiments.

5. Acknowledgements

These studies were supported by NSERC Discovery Grants to JVR (RGPIN-2016-371705) and CMY (RGPIN-2015-043), by a CIHR project grant to JVR (DOL 409157) and by a NSERC Research Tools and Instrumentation Grant (2018-00846) to JVR. We thank Yufeng Wang and Vidhant Pal for assistance with islet isolation expertise.

6. Competing Interests

The authors declare no competing interests.

7. References

Antonenkov, V. D. (1989). Dehydrogenases of the pentose phosphate pathway in rat liver peroxisomes. *European Journal of Biochemistry*, *183*(1), 75–82. https://doi.org/10.1111/j.1432-1033.1989.tb14898.x

Aston-Mourney, K., Wong, N., Kebede, M., Zraika, S., Balmer, L., McMahon, J. M., Fam, B. C., Favaloro, J., Proietto, J., Morahan, G., & Andrikopoulos, S. (2007). Increased nicotinamide nucleotide transhydrogenase levels predispose to insulin hypersecretion in a mouse strain susceptible to diabetes. *Diabetologia 2007 50:12*, *50*(12), 2476–2485. https://doi.org/10.1007/S00125-007-0814-X

Axelrod, D. (1979). Carbocyanine Dye Orientation in Red Cell Membrane Studied by Microscopic Fluorescence Polarization. *Biophysical Journal*, *26*(3), 557–573. https://doi.org/10.1016/S0006-3495(79)85271-6

Batenburg, J. J., & Olson, M. S. (1976). Regulation of Pyruvate Dehydrogenase by Fatty Acid in Isolated Rat Liver Mitochondria*. *Journal of Biological Chemistry*, *251*(5), 1364–1370. https://doi.org/10.1016/S0021-9258(17)33748-1

Bellomo, G., Vairetti, M., Stivala, L., Mirabelli, F., Richelmi, P., & Orrenius, S. (1992). Demonstration of nuclear compartmentalization of glutathione in hepatocytes. *Proceedings of the National Academy of Sciences of the United States of America*, *89*(10), 4412–4416. https://doi.org/10.1073/pnas.89.10.4412

Blackman, S. M., Cobb, C. E., Beth, A. H., & Piston, D. W. (1996). The Orientation of Eosin-5-Maleimide on Human Erythrocyte Band 3 Measured by Fluorescence Polarization Microscopy. *Biophysical Journal*, *71*(July), 194–208. https://doi.org/10.1016/S0006-3495(96)79216-0

Cameron, W. D., Bui, C. V, Hutchinson, A., Loppnau, P., Gräslund, S., & Rocheleau, J. V. (2016). Apollo-NADP+: a spectrally tunable family of genetically encoded sensors for NADP+. *Nature Methods*, *13*(4), 352–358. https://doi.org/10.1038/nmeth.3764

Cline, G. W., LePine, R. L., Papas, K. K., Kibbey, R. G., & Shulman, G. I. (2004). 13C NMR isotopomer analysis of anaplerotic pathways in INS-1 cells. *Journal of Biological Chemistry*, *279*(43), 44370–44375. https://doi.org/10.1074/jbc.M311842200

Crameri, F. (2018). *Scientific colour-maps*. https://doi.org/10.5281/ZENODO.1287763

Cunningham, A. D., Colavin, A., Huang, K. C., & Mochly-Rosen, D. (2017). Coupling between Protein Stability and Catalytic Activity Determines Pathogenicity of G6PD Variants. *Cell Reports*, *18*(11), 2592–2599. https://doi.org/10.1016/j.celrep.2017.02.048

Dzyakanchuk, A. A., Balázs, Z., Nashev, L. G., Amrein, K. E., & Odermatt, A. (2009). 11β-Hydroxysteroid dehydrogenase 1 reductase activity is dependent on a high ratio of NADPH/NADP+ and is stimulated by extracellular glucose. *Molecular and Cellular Endocrinology*, *301*(1–2), 137–141. https://doi.org/10.1016/j.mce.2008.08.009

Fergusson, G., Éthier, M., Guévremont, M., Chrétien, C., Attané, C., Joly, E., Fioramonti, X., Prentki, M., Poitout, V., & Alquier, T. (2014). Defective insulin secretory response to intravenous glucose in C57Bl/6J compared to C57Bl/6N mice. *Molecular Metabolism*, *3*(9), 848–854. https://doi.org/10.1016/J.MOLMET.2014.09.006

Frederiks, W. M., Vreeling-sindela, H., & Noorden, C. J. F. Van. (2007). Loss of Peroxisomes Causes Oxygen Insensitivity of the Histochemical Assay of Glucose-6-Phosphate Dehydrogenase Activity to Detect Cancer Cells. *Journal of Histochemistry & Cytochemistry*, *55*(2), 175–181. https://doi.org/10.1369/jhc.6A7068.2006

Freeman, H. C., Hugill, A., Dear, N. T., Ashcroft, F. M., & Cox, R. D. (2006). Deletion of Nicotinamide Nucleotide Transhydrogenase. *Diabetes*, *55*(7), 2153–2156. https://doi.org/10.2337/DB06-0358

Geisbrecht, B. V, & Gould, S. J. (1999). The Human PICD Gene Encodes a Cytoplasmic and Peroxisomal NADP+-dependent Isocitrate Dehydrogenase. *The Journal of Biological*

Chemistry, *274*(43), 30527–30533.

Goedhart, J., Stetten, D. Von, Noirclerc-savoye, M., Lelimousin, M., Joosen, L., Hink, M. A., Weeren, L. Van, Jr, T. W. J. G., & Royant, A. (2012). Structure-guided evolution of cyan fluorescent proteins towards a quantum yield of 93%. *Nature Communications*. https://doi.org/10.1038/ncomms1738

Goedhart, J., Von Stetten, D., Noirclerc-Savoye, M., Lelimousin, M., Joosen, L., Hink, M. A., Van Weeren, L., Gadella, T. W. J., & Royant, A. (2012). Structure-guided evolution of cyan fluorescent proteins towards a quantum yield of 93%. *Nature Communications 2012 3:1*, *3*(1), 1–9. https://doi.org/10.1038/ncomms1738

Gould, S. J., Keller, G.-A., Hosken, N., Wilkinson, J., & Subramani, S. (1989). A Conserved Tripeptide Sorts Proteins to Peroxisomes. *Journal of Cell Biology*, *108*(5), 1657–1664.

Haythorne, E., Rohm, M., van de Bunt, M., Brereton, M. F., Tarasov, A. I., Blacker, T. S., Sachse, G., Silva dos Santos, M., Terron Exposito, R., Davis, S., Baba, O., Fischer, R., Duchen, M. R., Rorsman, P., MacRae, J. I., & Ashcroft, F. M. (2019). Diabetes causes marked inhibition of mitochondrial metabolism in pancreatic β-cells. *Nature Communications*, *10*(1), 1–17. https://doi.org/10.1038/s41467-019-10189-x

Jankowski, A., Kim, J. H., Collins, R. F., Daneman, R., Walton, P., & Grinstein, S. (2001). In Situ Measurements of the pH of Mammalian Peroxisomes Using the Fluorescent Protein pHluorin. *The Journal of Biological Chemistry*, *276*(52), 48748–48763. https://doi.org/10.1074/jbc.M109003200

Jensen, M. V, Joseph, J. W., Ronnebaum, S. M., Burgess, S. C., Sherry, A. D., & Newgard, C. B. (2008). Metabolic cycling in control of glucose-stimulated insulin secretion. *Am J Physiol Endocrinol Metab*, *295*, 1287–1297. https://doi.org/10.1152/ajpendo.90604.2008.

Khan, A., Ling, Z. C., & Landau, B. R. (1996). Quantifying the carboxylation of pyruvate in pancreatic islets. *Journal of Biological Chemistry*, *271*(5), 2539–2542. https://doi.org/10.1074/jbc.271.5.2539

Lambert, T. J. (2019). FPbase: a community-editable fluorescent protein database. In *Nature Methods* (Vol. 16, Issue 4, pp. 277–278). Nature Publishing Group. https://doi.org/10.1038/s41592-019-0352-8

Lee, J., Choi, A. H., Ham, M., Kim, J., Choe, S. S., Park, J., Lee, G. Y., Yoon, K., & Kim, J. B. (2011). G6PD Up-Regulation Promotes Pancreatic B-Cell Dysfunction. *Endocrinology*, *152*(March), 793–803. https://doi.org/10.1210/en.2010-0606

Llopis, J., Mccaffery, J. M., Miyawaki, A., Farquhar, M. G., & Tsien, R. Y. (1998). Measurement of Cytosolic , Mitochondrial , and Golgi pH in Single Living Cells with Green Fluorescent Proteins. *Cell Biology*, *95*, 6803–6808.

Loiselle, F. B., & Casey, J. R. (2010). Measurement of Intracellular pH. *Methods in Molecular Biology (Clifton, N.J.)*, *637*, 311–331. https://doi.org/10.1007/978-1-60761-700-6_17

Lu, D., Mulder, H., Zhao, P., Burgess, S. C., Jensen, M. V., Kamzolova, S., Newgard, C. B., & Sherry, A. D. (2002). 13C NMR isotopomer analysis reveals a connection between pyruvate cycling and glucose-stimulated insulin secretion (GSIS). *Proceedings of the National Academy of Sciences of the United States of America*, *99*(5), 2708–2713. https://doi.org/10.1073/pnas.052005699

MacDonald, M. J. (1995). Feasibility of a mitochondrial pyruvate malate shuttle in pancreatic islets. Further implication of cytosolic NADPH in insulin secretion. *Journal of Biological Chemistry*, *270*(34), 20051–20058. https://doi.org/10.1074/jbc.270.34.20051

MacDonald, Michael J. (1993). Estimates of Glycolysis, Pyruvate (De)Carboxylation, Pentose

Phosphate Pathway, and Methyl Succinate Metabolism in Incapacitated Pancreatic Islets. *Archives of Biochemistry and Biophysics*, *305*(2), 205–214.

Mahato, R. I., Smith, L. C., & Rolland, A. (1999). Pharmaceutical Perspectives of Nonviral Gene Therapy. In J. C. Hall, J. C. Dunlap, T. Friedmann, & F. Gianelli (Eds.), *Advances in Genetics* (41st ed., pp. 95–156). Acadenuc Press.

Matschinsky, F., Liang, Y., Kesavan, P., Wang, L., Froguel, P., Velho, G., Cohen, D., Alan, M., Tanizawa, Y., Jetton, T. L., Niswender, K., & Magnuson, M. A. (1993). Glucokinase as Pancreatic B Cell Glucose Sensor and Diabetes Gene. *J. Clin. Invst.*

Minard, K. I., & McAlister-Henn, L. (1999). Dependence of peroxisomal β-oxidation on cytosolic sources of NADPH. *Journal of Biological Chemistry*, *274*(6), 3402–3406. https://doi.org/10.1074/jbc.274.6.3402

Ming, A. Y. K., Yoo, E., Vorontsov, E. N., Altamentova, S. M., Kilkenny, D. M., & Rocheleau, J. V. (2012). Dynamics and distribution of Klothoβ (KLB) and Fibroblast Growth Factor Receptor-1 (FGFR1) in living cells reveal the Fibroblast Growth Factor-21 (FGF21)-induced receptor complex. *Journal of Biological Chemistry*, *287*(24), 19997–20006. https://doi.org/10.1074/jbc.M111.325670

Moon, S. J., Dong, W., Stephanopoulos, G. N., & Sikes, H. D. (2020). Oxidative pentose phosphate pathway and glucose anaplerosis support maintenance of mitochondrial NADPH pool under mitochondrial oxidative stress. *Bioengineering & Translational Medicine*, *5*(3), e10184. https://doi.org/10.1002/btm2.10184

Newgard, C. B., & McGarry, J. D. (1995). Metabolic Coupling Factors in Pancreatic B-Cell Signal Transduction. *Annu. Rev. Biochem.*, *64*, 689–719.

Okumoto, K., Tamura, S., Honsho, M., & Fujiki, Y. (2020). Peroxisome: Metabolic Functions and Biogenesis. In *Advances in Experimental Medicine and Biology* (Vol. 1299, pp. 3–17). Springer. https://doi.org/10.1007/978-3-030-60204-8_1

Orij, R., Postmus, J., Beek, A. Ter, Brul, S., & Smits, G. J. (2009). In vivo measurement of cytosolic and mitochondrial pH using a pH-sensitive GFP derivative in Saccharomyces cerevisiae reveals a relation between intracellular pH and growth. *Microbiology*, *155*, 268–278. https://doi.org/10.1099/mic.0.022038-0

Pal, V., Wang, Y., Regeenes, R., Kilkenny, D. M., & Rocheleau, J. V. (2022). Laminin matrix regulates beta-cell FGFR5 expression to enhance glucose-stimulated metabolism. *Scientific Reports*. https://doi.org/10.1038/s41598-022-09804-7

Pallardó, F. V., Markovic, J., García, J. L., & Viña, J. (2009). Role of nuclear glutathione as a key regulator of cell proliferation. In *Molecular Aspects of Medicine* (Vol. 30, Issues 1–2, pp. 77–85). Pergamon. https://doi.org/10.1016/j.mam.2009.01.001

Patel, B. N., Mackness, M. I., & Connock, M. J. (1987). Peroxisomal localization of glucose-6-phosphate dehydrogenase and pyrophosphate-stimulated dihydroxyacetone-phosphate acyltransferase in mouse kidney. *Biochemical Journal*, *244*(2), 443–448. https://doi.org/10.1042/bj2440443

Poburko, D., Santo-domingo, J., & Demaurex, N. (2011). Dynamic Regulation of the Mitochondrial Proton Gradient during Cytosolic Calcium Elevations. *The Journal of Biological Chemistry*, *286*(13), 11672–11684. https://doi.org/10.1074/jbc.M110.159962

Pongratz, R. L., Kibbey, R. G., Shulman, G. I., & Cline, G. W. (2007). Cytosolic and Mitochondrial Malic Enzyme Isoforms Differentially Control Insulin Secretion. *The Journal of Biological Chemistry*, *282*(1), 200–207. https://doi.org/10.1074/jbc.M602954200

Pullen, T. J., Khan, A. M., Barton, G., Butcher, S. A., Sun, G., & Rutter, G. A. (2014).

Identification of genes selectively disallowed in the pancreatic islet Identification of genes selectively disallowed in the pancreatic islet. *Islets*, *2*(2), 89–95. https://doi.org/10.4161/isl.2.2.11025

Regeenes, R., Silva, P. N., Chang, H. H., Arany, E. J., Shukalyuk, A. I., Audet, J., Kilkenny, D. M., & Rocheleau, J. V. (2018). Fibroblast growth factor receptor 5 (FGFR5) is a co-receptor for FGFR1 that is up-regulated in beta-cells by cytokine-induced inflammation. *Journal of Biological Chemistry*. https://doi.org/10.1074/jbc.RA118.003036

Rocheleau, J. V, Edidin, M., & Piston, D. W. (2003). Intrasequence GFP in Class I MHC Molecules , a Rigid Probe for Fluorescence Anisotropy Measurements of the Membrane Environment. *Biophysical Journal*, *84*(June), 4078–4086.

Ronnebaum, S. M., Ilkayeva, O., Burgess, S. C., Joseph, J. W., Lu, D., Stevens, R. D., Becker, T. C., Sherry, A. D., Newgard, C. B., & Jensen, M. V. (2006). A Pyruvate Cycling Pathway Involving Cytosolic NADP-dependent Isocitrate Dehydrogenase Regulates Glucose-stimulated Insulin Secretion. *The Journal of Biological Chemistry*, *281*(41), 30593–30602. https://doi.org/10.1074/jbc.M511908200

Ross, B. L., Tenner, B., Markwardt, M. L., Zviman, A., Shi, G., Kerr, J. P., Snell, N. E., Mcfarland, J. J., Mauban, J. R., Ward, C. W., Rizzo, M. A., & Zhang, J. (2018). Single-color, ratiometric biosensors for detecting signaling activities in live cells. *ELife*, 1–15.

Rydström, J. (1972). Site-specific inhibitors of mitochondrial nicotinamide-nucleotide transhydrogenase. *European Journal of Biochemistry*, *31*(3), 496–504. https://doi.org/10.1111/J.1432-1033.1972.TB02557.X

Rydström, J. (2006). Mitochondrial NADPH, transhydrogenase and disease. In *Biochimica et Biophysica Acta - Bioenergetics* (Vol. 1757, Issues 5–6, pp. 721–726). Biochim Biophys Acta. https://doi.org/10.1016/j.bbabio.2006.03.010

Schuit, F., De Vos, A., Farfari, S., Moens, K., Pipeleers, D., Brun, T., & Prentki, M. (1997a). Metabolic fate of glucose in purified islet cells. Glucose-regulated anaplerosis in β cells. *Journal of Biological Chemistry*, *272*(30), 18572–18579. https://doi.org/10.1074/jbc.272.30.18572

Schuit, F., De Vos, A., Farfari, S., Moens, K., Pipeleers, D., Brun, T., & Prentki, M. (1997b). Metabolic Fate of Glucose in Purified Islet Cells: GLUCOSE-REGULATED ANAPLEROSIS IN β CELLS. *Journal of Biological Chemistry*, *272*(30), 18572–18579. https://doi.org/10.1074/JBC.272.30.18572

Schuit, F., Vos, A. De, Farfari, S., Moens, K., Pipeleers, D., Brun, T., & Prentki, M. (1997). Metabolic Fate of Glucose in Purified Islet Cells. *The Journal of Biological Chemistry*, *272*(30), 18572–18579.

Smolková, K., & Ježek, P. (2012). The role of mitochondrial NADPH-dependent isocitrate dehydrogenase in cancer cells. In *International Journal of Cell Biology*. https://doi.org/10.1155/2012/273947

Stanton, R. C. (2012). Glucose-6-Phosphate Dehydrogenase, NADPH, and Cell Survival. *IUBMB Life*, *64*(5), 362–369. https://doi.org/10.1016/j.tcb.2018.03.003

Sun, M. Y., Yoo, E., Green, B. J., Altamentova, S. M., Kilkenny, D. M., & Rocheleau, J. V. (2012). Autofluorescence imaging of living pancreatic islets reveals fibroblast growth factor-21 (FGF21)-induced metabolism. *Biophysical Journal*, *103*(11), 2379–2388. https://doi.org/10.1016/j.bpj.2012.10.028

Tao, R., Zhao, Y., Chu, H., Wang, A., Zhu, J., Chen, X., Zou, Y., Shi, M., Liu, R., Su, N., Du, J., Zhou, H.-M., Zhu, L., Qian, X., Liu, H., Loscalzo, J., & Yang, Y. (2017). Genetically encoded

fluorescent sensors reveal dynamic regulation of NADPH metabolism. *Nature Methods*, *14*(April). https://doi.org/10.1038/nmeth.4306

Tiedge, M., Lortz, S., Drinkgern, J., & Lenzen, S. (1997). Relation Between Antioxidant Enzyme Gene Expression and Antioxidative Defense Status of Insulin-Producing Cells. *Diabetes*, *46*(46).

Toye, A. A., Lippiat, J. D., Proks, P., Shimomura, K., Bentley, L., Hugill, A., Mijat, V., Goldsworthy, M., Moir, L., Haynes, A., Quarterman, J., Freeman, H. C., Ashcroft, F. M., & Cox, R. D. (2005). A genetic and physiological study of impaired glucose homeostasis control in C57BL/6J mice. *Diabetologia 2005 48:4*, *48*(4), 675–686. https://doi.org/10.1007/S00125-005-1680-Z

Tran, D. H., Kesavan, R., Rion, H., Soflaee, M. H., Solmonson, A., Bezwada, D., Vu, H. S., Cai, F., Phillips, J. A., DeBerardinis, R. J., & Hoxhaj, G. (2021). Mitochondrial NADP+ is essential for proline biosynthesis during cell growth. *Nature Metabolism*, *3*(4), 571–585. https://doi.org/10.1038/s42255-021-00374-y

Vogel, R., Wiesinger, H., Hamprecht, B., & Dringen, R. (1999). The regeneration of reduced glutathione in rat forebrain mitochondria identifies metabolic pathways providing the NADPH required. *Neuroscience Letters*, *275*(2), 97–100. https://doi.org/10.1016/S0304-3940(99)00748-X

Warren, S. C., Margineanu, A., Katan, M., Dunsby, C., & French, P. M. W. (2015). Homo-FRET Based Biosensors and Their Application to Multiplexed Imaging of Signalling Events in Live Cells. *International Journal of Molecular Sciences*, *16*, 14695–14716. https://doi.org/10.3390/ijms160714695

Wu, M. M., Llopis, J., Adams, S., Mccaffery, J. M., Kulomaa, M. S., Machen, T. E., Moore, H. H., & Tsien, R. Y. (2000). Organelle pH studies using targeted avidin and fluorescein – biotin. *Cell Chemistry Biology*, *7*(3), 197–209.

Ying, W. (2008). NAD+/NADH and NADP+/NADPH in Cellular Functions and Cell Death: Regulation and Biological Consequences. *Antioxidants & Redox Signaling*, *10*(2). https://doi.org/10.1089/ars.2007.1672

Zhang, G. F., Jensen, M. V., Gray, S. M., El, K., Wang, Y., Lu, D., Becker, T. C., Campbell, J. E., & Newgard, C. B. (2021). Reductive TCA cycle metabolism fuels glutamine- and glucose-stimulated insulin secretion. *Cell Metabolism*, *33*(4), 804-817.e5. https://doi.org/10.1016/j.cmet.2020.11.020

Zhang, Z., Liew, C. W., Handy, D. E., Zhang, Y., Leopold, J. A., Hu, J., Guo, L., Kulkarni, R. N., Loscalzo, J., & Stanton, R. C. (2010). High glucose inhibits glucose-6-phosphate dehydrogenase , leading to increased oxidative stress and B-cell apoptosis. *The FASEB Journal*, *24*, 1497–1505. https://doi.org/10.1096/fj.09-136572